ARTICLE   OPEN

Check for updates

Flexible aqueous Zn–S battery based on an S-decorated Ti$_3$C$_2$T$_x$ cathode

Keval K. Sonigara[1], Jayraj V. Vaghasiya [2], Carmen C. Mayorga-Martinez [2] and Martin Pumera [1,2,3,4✉]

Flexible aqueous zinc-ion batteries can store energy safely and at a low cost, which benefits wearable electronic gadgets; however, currently used cathodes restrict these devices with a low specific capacity and energy density. Herein, we developed a flexible zinc-sulfur (Zn–S) battery constructed by Ti$_3$C$_2$T$_x$ decorated with sulfur (S@Ti$_3$C$_2$T$_x$) as a cathode and Zn metal anode with iodine-added amphiphilic gel electrolyte (AGE). Benefiting from the confinement synergy of S@Ti$_3$C$_2$T$_x$ cathode, the Zn-S battery exhibited a high storage capacity of 772.7 mAh g^{-1} at 300 mA g^{-1}, which is higher than a conventional S-decorated carbon cathode (491.7 mAh g^{-1}). More specially, the flexible device offers good cycling stability (82.7%) and excellent mechanical stability with 91% capacity retention after 90° bending (500 cycles). To demonstrate real applications, the flexible Zn–S batteries were integrated in series to power electrical gadgets (e.g., digital clock, light-emitting diode, and robot). It exhibits exceptional flexibility to sustain different deformations and maintains a steady supply of power to run the wearable electronic gadget. These findings offer a fresh starting point for flexible energy storage technologies and show the promising potential of the Zn–S battery in real-world applications.

INTRODUCTION

The aqueous zinc-ion battery (ZIB) emerges as a sustainable energy storage device due to its low-cost components and environmental friendliness[1–4]. It is also the most investigated flexible energy storage device due to its safe wearability. However, many ZIB devices are constructed using metal oxide-/polymer-based intercalation-type cathodes (e.g., Mn, Ni, Ti, V, and polyaniline)[5–8], which limits their performance due to their low theoretical capacity. Recently, sulfur (S) cathodes emerged as an inexpensive alternative to the above cathodes in ZIBs due to their low-cost, high theoretical conversion capacity, and safe Zn–S conversion potential in aqueous electrolytes[9–12]. However, Zn–S batteries are still underperforming in terms of conversion kinetics and stability due to the insulating nature of sulfur, sluggish Zn–S conversion reaction, and the formation of byproducts that result in the loss of active material[13,14]. To overcome the above issues, a few attempts have been reported to improve the performance of sulfur cathodes by confining composites with porous carbon[15,16], carbon nanotubes[17], carbon nanofibers[18], Fe(CN)$_6^{4-}$-doped polyaniline[19], S@FeN$_4$ single sites/nitrogen-doped carbon[20], and sulfur in ionic liquid films[21]. Along with this, efforts have also been made with modifications in electrolytes, i.e., adding catalytic iodine redox additive[17], mixing urea as a co-mediator[22], solvation agent strategy by using eutectic electrolyte[23], and using co-solvents like tetraglyme[24] and ethylene glycol[18,25]. These efforts successfully improved the reversibility of Zn–S conversion with a reduced energy barrier.

To make the Zn–S battery a versatile component, more effort is needed to implement efficient cathode confinement with advanced strategies and solid/gel-type electrolytes instead of liquid electrolytes that could serve to develop future flexible batteries. Recently, the two-dimensional (2D) transition metal

carbide (MXenes) materials have emerged as potential electrodes and conductive confinement materials to improve cathode performance in ZIBs due to their high conductivity, large surface area, and diverse surface functionalities[26,27]. The model MXene, Ti$_3$C$_2$T$_x$, was found as an efficient buffer medium to increase Zn^{2+} storage in polyaniline cathodes due to its 2D nanosheet morphology, which provides a platform for fast diffusion pathways[28]. The confinement of MXenes (e.g., Ti$_3$C$_2$T$_x$ and V$_2$CT$_x$) with various metal oxide composite cathodes (e.g., MnO$_2$[29], V$_2$O$_5$[30,31], ZnMn$_2$O$_4$[32], and H$_2$V$_3$O$_8$[33]) greatly improved the intercalation performance in ZIBs by enhanced conductivity and the impact of surface groups. Li et al. reported aqueous I$_2$/I$^-$ redox kinetics boosted by MXene conductive confinement for Zn-I$_2$ conversion chemistry benefited from the confinement effect and faster charge transfer[34]. Looking at the versatility of MXenes, it is possible to design an MXene-confined sulfur cathode composite that will enhance the Zn–S battery's chemistry by providing conductive confinement to the sulfur cathode and increasing the activity of redox additives like iodide–triiodide.

Developing a flexible Zn–S battery with high performance. Herein, we prepared a flexible Zn–S battery using S@Ti$_3$C$_2$T$_x$ as cathode and AGE as gel electrolyte. The 2D morphology and metallic property of Ti$_3$C$_2$T$_x$ offer conductive confinement to the sulfur cathode for improved Zn–S redox kinetics and quick diffusion paths to the Zn^{2+} ions. On the other hand, the amphiphilic nature of AGE helps to develop robust interfaces with electrodes and restricts the shuttle of iodide species so they can benefit from regulated self-discharge. The as-fabricated Zn–S battery with S@Ti$_3$C$_2$T$_x$ cathode offers high power capacity, good cycling stability, and excellent capacity retention upon multiple bending modes. To demonstrate a real application, the Zn–S batteries were connected in series to power a digital clock, red-

[1]Future Energy and Innovation Laboratory, Central European Institute of Technology, Brno University of Technology, Brno, Czech Republic. [2]Center for Advanced Functional Nanorobots, Department of Inorganic Chemistry, Faculty of Chemical Technology, University of Chemistry and Technology Prague, Prague, Czech Republic. [3]Faculty of Electrical Engineering and Computer Science, VSB - Technical University of Ostrava, Ostrava, Czech Republic. [4]Department of Medical Research, China Medical University Hospital, China Medical University, Taichung, Taiwan. ✉email: pumera.research@gmail.com

npj
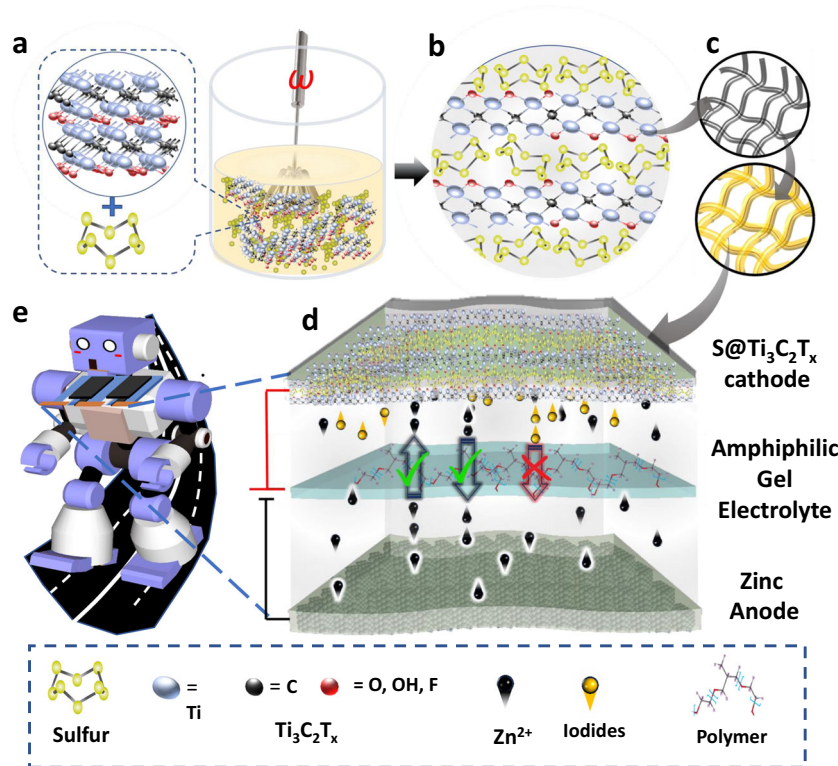
Fig. 1 Schematic illustration of preparing flexible Zn-S battery cathode based on S@Ti₃C₂Tₓ for powering a down-scaled robot.
a Synthesis of S@Ti₃C₂Tₓ by solution shear-assisted method. **b** Molecular schematic of S@Ti₃C₂Tₓ composite. **c** Deposition on carbon cloth. **d** Flexible Zn–S battery with S@Ti₃C₂Tₓ cathode, Zn anode, and amphiphilic gel electrolyte-infused cellulose as a separator. **e** Down-scaled robot powered by the produced wearable Zn–S battery.

light-emitting diode, and robot to provide a steady power supply in various deformations. To the best of our knowledge, this is an exclusive work of a Ti₃C₂Tₓ-assisted flexible Zn-S (aqueous) battery has been reported.

RESULTS AND DISCUSSIONS

Synthesis and morphology study of S@Ti₃C₂Tₓ

To develop an efficient cathode electrode, S@Ti₃C₂Tₓ was prepared by liquid shear in situ sulfur decoration of exfoliated Ti₃C₂Tₓ in the presence of surfactant by strong mechanical blending (Fig. 1a). More details are given in the experimental section. This method avoids energy-consuming high-temperature methods, which are commonly used to blend S with host materials[15–17]. After that, carbon cloth was used as a conductive substrate to create a flexible S@Ti₃C₂Tₓ cathode electrode (Fig. 1b, c). Finally, a flexible aqueous Zn–S battery was developed by employing S@Ti₃C₂Tₓ as a cathode, Zn foil as an anode, and AGE as an electrolyte, which shows significant applications to power various electronic devices (Fig. 1d, e). The battery works with a reported hybrid mechanism[17,24] during the discharge process: $Zn^{2+} + S + I_3^- + 4e^- \rightarrow ZnS + 3I^-$ and during the charging process, $ZnS + 3I^- \rightarrow I_3^- + S + Zn^{2+} + 4e^-$. Here, the proposed highly conductive Ti₃C₂Tₓ as cathode composite provides confinement synergy to activate the insulated sulfur and iodine for faster and facile redox reactions and alleviate the conductive channels for Zn ion diffusion. On the other side, the ethylene oxide and propylene oxide groups of the AGE matrix allow the good dissolution of iodine and also restrict the diffusion of iodides[35,36]. Before examining the S@Ti₃C₂Tₓ cathode's role in flexible Zn–S batteries and their actual application to power electrical devices, it is crucial to first look at the structural, morphological, and electrochemical properties of S@Ti₃C₂Tₓ composite and AGE. Here, the S@Ti₃C₂Tₓ composite was characterized

systematically by thermogravimetric analysis (TGA), X-ray diffraction (XRD), scanning electron microscopy (SEM), scanning transmission electron microscopy (STEM), energy-dispersive X-ray spectroscopy (EDS), transmission electron microscopy (TEM), and high-resolution scanning transmission electron microscopy (HR-STEM) to validate the successive composition preparation.

The SEM image of pristine Ti₃C₂Tₓ in Fig. 2a shows an ordered arrangement of 2D nanosheet stack clusters with a size of ~5–6 μm length and a visible gap between the sheets. The EDS elementary mapping (Supplementary Fig. 1) of these nanosheet stacks confirms the presence of elements Ti, C, F, and O. Further, solution-sheared Ti₃C₂Tₓ was analyzed by STEM and found to contain well-dispersed Ti₃C₂Tₓ nanosheets (Fig. 2b) similar in size to the stacks. TEM and HR-TEM images (Fig. 2c, d) of few-layer nanosheets show good crystallinity as confirmed by selected area electron diffraction (SAED, inset of Fig. 2d), indicating neat splits in the Ti₃C₂Tₓ stacks during solution shearing. The STEM image and corresponding EDS elementary mapping of sheared S@Ti₃C₂Tₓ are presented in Fig. 2e. We can see clearly that S is evenly attached to the surface of the Ti₃C₂Tₓ nanosheets, creating a uniform S@Ti₃C₂Tₓ layer structure. The EDS mappings validated the presence of S, Ti, and C distribution.

TGA analysis conducted under a nitrogen atmosphere estimated the sulfur proportion of ~60 wt% in the composite prepared using the solution shearing method (Supplementary Fig. 2). XRD was used to examine the crystalline properties of S@Ti₃C₂Tₓ composites (Supplementary Fig. 3). The XRD pattern of Ti₃C₂Tₓ indicates the broad diffraction peak at $2\theta = \sim 8°$ (002), representing the efficient splits of nanosheets through the shearing method[28]. In the composite samples, Ti₃C₂Tₓ peaks emerge in strong peaks of S and the representative peak of Ti₃C₂Tₓ, still visible below $2\theta = 8°$, indicates a large distance between the Ti₃C₂Tₓ nanosheets by effective in situ S decoration.
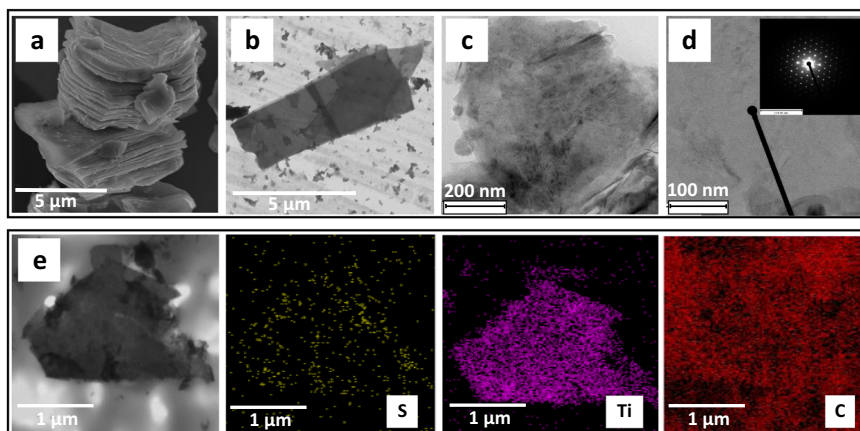
Fig. 2 Morphology study. a SEM image of pristine $Ti_3C_2T_x$. **b** STEM image of sheared $Ti_3C_2T_x$ nanosheet. **c** TEM image of $Ti_3C_2T_x$ nanosheet. **d** HR-TEM image of $Ti_3C_2T_x$ nanosheet (inset represents SAED pattern). **e** STEM of sheared S@$Ti_3C_2T_x$ and corresponding EDS elementary mapping.

XRD study suggests an effective physical blending of $Ti_3C_2T_x$ with S without oxidation or chemical reactions. The quality and extent of the S@$Ti_3C_2T_x$ can be studied from the surface area of the materials. BET analysis of $Ti_3C_2T_x$ and S@$Ti_3C_2T_x$ was carried out to study the specific surface area, which is an important parameter for the quality of electrodes. The adsorption–desorption isotherm of both materials is provided in Supplementary Fig. 4. It is noticed that the surface area of $Ti_3C_2T_x$ was 17.34 $m^2\,g^{-1}$, which decreased when blended with S (10.04 $m^2\,g^{-1}$), thus confirming the compact physical morphology of the cathode's composition[37]. This can be beneficial for better diffusion of Zn ions by improved conductivity in the presence of $Ti_3C_2T_x$ and good adsorption of iodides during charge–discharge.

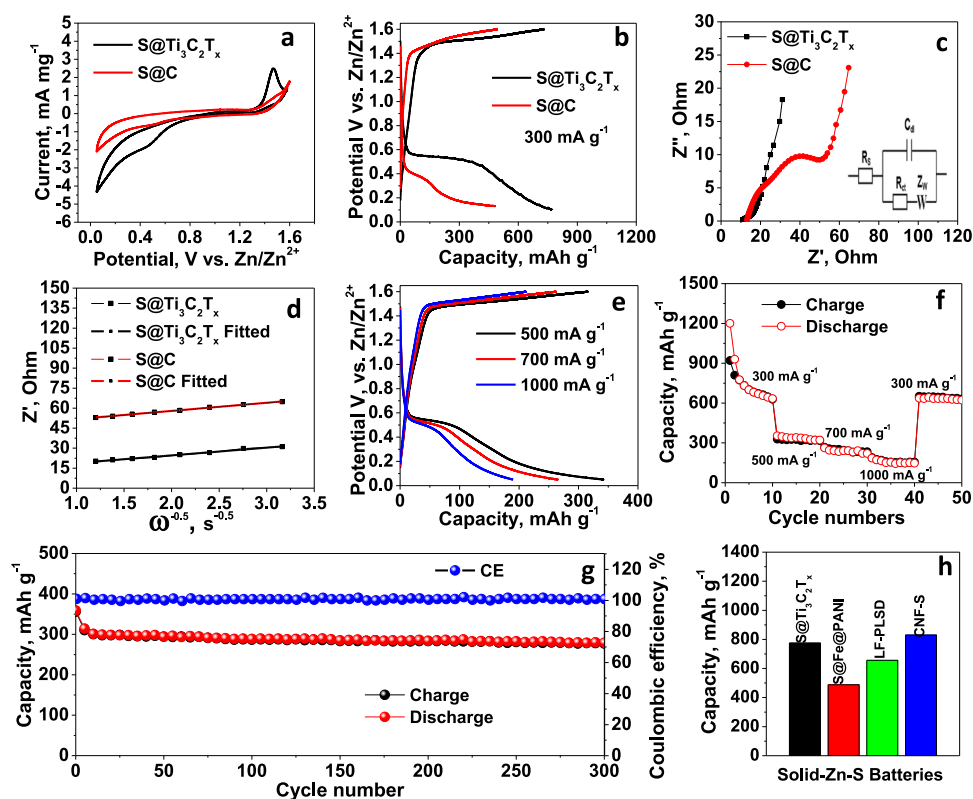## Electrochemical storage study of S@$Ti_3C_2T_x$

When improving the electrochemical storage capabilities of prepared S@$Ti_3C_2T_x$ cathodes with an aqueous system, the selection of the current collector and electrolyte is very important. In the present case, we have adopted hydrophobic carbon cloth as a current collector due to the non-polar properties of elemental sulfur. The electrolyte developed here with zinc acetate, iodine, and the block copolymer is amphiphilic and possesses a sol–gel-type nature to ensure good interfacial contact formation (Supplementary Fig. 5a); this is inspired by polymer hydrogel electrolyte from pluronic polymer, which proved excellent for ZIBs[38]. To confirm the interfacial compatibility of the cathode, we compared the optical observation of a drop of liquid electrolyte on top of carbon cloth coated with pristine $Ti_3C_2T_x$ and S@$Ti_3C_2T_x$. The electrode surface of S@$Ti_3C_2T_x$ composition becomes highly hydrophobic compared to the former and seems inconvenient for the system (Supplementary Fig. 5b). The issue is solved by the compact interface created due to the AGE electrolyte's amphiphilic and thermo-reversible properties, which allows it to be well-wetted on the S@$Ti_3C_2T_x$ cathode in the sol phase before turning into a gel (Supplementary Fig. 5b). AGE is also responsible for the facile dissolution of iodine due to the presence of polymer in the matrix; hence, it helps form a facile I^-/I_3^- redox couple. Supplementary Figure 6 shows the nature of iodine dissolution in comparison to electrolytes with and without polymer and reveals a clear solution with polymer by faster dissolution. The AGE maintains good ionic conductivity of 4.01 S cm^{-1} (Supplementary Fig. 7 and supplementary equation 1) and shows a zinc-ion transference number of 0.45 measured from DC polarization between zinc-blocking electrodes (Supplementary Fig. 8 and supplementary equation 2). The zinc stripping–plating cycles of AGE conducted between symmetrical zinc electrodes result in a

stabilized voltage profile for 100 cycles, indicating the good electrochemical suitability of AGE (Supplementary Fig. 9). Notably, AGE also shows a wide electrochemical operational voltage window up to 2.0 V vs. Zn suitable for safe aqueous systems (Supplementary Figure 10). Further, the gel property of AGE also benefits the flexibility of the device[39].

To evaluate the electrochemical performance of S@$Ti_3C_2T_x$ and S@C (S confined with carbon nanopowder) cathodes, three-electrode cyclic voltammetry (CV) was conducted in the I^-/I_3^- solution (Supplementary Fig. 11). It is observed that both S cathodes show reversible redox peaks of I^-/I_3^-, similarly referenced to glassy carbon electrodes. Besides, reduced current density was observed on both cathodes due to the presence of insulating S. However, S@$Ti_3C_2T_x$ shows a higher electrochemical response with low polarization compared to S@C, which indicates the superior conductivity and surface of S@$Ti_3C_2T_x$. Further, Zn–S batteries were fabricated in CR2032 coin cells with the configuration of Zn/AGE-cellulose separator/S@$Ti_3C_2T_x$-carbon cloth. The fabricated device builds up a stable open circuit potential (OCP) of 1.068 ± 0.010 V vs. Zn/Zn^{2+}, slightly deviating from the theoretical OCP of the Zn–S system explained elsewhere (1.044 V vs. Zn^{2+}/Zn)[23]. This deviation may be assigned to the composite contribution of a modified cathode and electrolyte system. Figure 3a shows the CV scans of the cathodes S@$Ti_3C_2T_x$ and S@C between 0.05 and 1.6 V at 0.1 mV s^{-1} scan speed, revealing a battery-type quasi-reversible characteristic. The cathodic peak recorded at 0.5 V vs. Zn/Zn^{2+} belongs to the ZnS formation and the anodic peak at 1.47 V vs. Zn/Zn^{2+} is for the reformation of sulfur from ZnS in aqueous electrochemistry[19,24]. The redox peaks of S@$Ti_3C_2T_x$ are sharp and include a large storage area compared to broad and reduced S@C peaks, indicating the superior confinement effect and faster zinc conversion storage.

Figure 3b illustrates the galvanostatic charging–discharging (GCD) voltage profile of both electrodes with similar voltage range at a current density of 300 mA g^{-1}. The S@$Ti_3C_2T_x$ delivered higher Zn storage and an improved electrochemical profile with a lower polarization voltage window compared to the carbon scaffold. The delivered specific capacity of S@$Ti_3C_2T_x$ is 772.7 mAh g^{-1}, which is higher than the conventional S@C cathode (491.7 mAh g^{-1}). Here, $Ti_3C_2T_x$ could provide a better-conducting environment and Zn ion transport flux that leads the enhanced storage performance. The capacity of the S@$Ti_3C_2T_x$/AGE-based device is improved compared to available reports of gel-based Zn-S battery as listed in Fig. 3h[18,19,21] and also reaches an impressive energy density of 363.16 Wh kg^{-1}, which is above the reported solid-state ZIBs[38–43]. Supplementary Figure 12 enlists the capacity of various reported MXene-supported cathodes for the ZIBs[28–34,40–43] as S@$Ti_3C_2T_x$ cathodes break the specific capacity limitation of such cathodes.

Fig. 3 Electrochemical study of S@Ti₃C₂Tₓ cathodes in Zn-S battery. a CV of S@Ti₃C₂Tₓ and S@C electrode at a scan rate of 0.1 mV s⁻¹ and **b** GCD curves at 300 mA g⁻¹. **c**, **d** Nyquist plots of S@Ti₃C₂Tₓ and S@C, and corresponding characteristic of Z_{real} to high-frequency relationship. **e**, **f** GCD curves of S@Ti₃C₂Tₓ at different rates and rate capability. **g** Stability measurement of S@Ti₃C₂Tₓ at 500 mA g⁻¹ for 300 cycles. **h** Comparison of the specific capacity performance of S@Ti₃C₂Tₓ at 300 mA g⁻¹ with reported Zn–S batteries with gel electrolytes.

This indicates that the combination of S and MXene can be a promising high-capacity cathode compared to other combinations with MXenes.

To understand the redox kinetics in these two different environments, the charge transfer and ion diffusion in the electrode are studied using electrochemical impedance spectroscopy (EIS). The obtained Nyquist plots from EIS are shown in Fig. 3c and the inset is the Randles equivalent circuit used to extract the resistance parameters[44]. The S@Ti₃C₂Tₓ cathode electrode shows low bulk resistance ($R_s = 11.12\,\Omega$) and charge transfer resistance ($R_{ct} = 16.83\,\Omega$), whereas the S@C electrode shows $R_s = 14.77\,\Omega$ and $R_{ct} = 45.47\,\Omega$, indicating a good conductive platform and faster charge transfer in MXene confinement. The kinetics of Zn²⁺ ions in the electrode matrix can be estimated by the Warburg factor, which is obtained from the relationship of Z_{real} and the low-frequency region of the EIS spectrum reflected as a straight line[44]. Figure 3d illustrates the relationship between Z_{real} and the low-frequency region of the EIS spectrum, and the slope of this graph is the Warburg factor based on supplementary equations (3) and (4) in the Supplementary Information, and it is inversely proportional to the diffusion. The lower value of the Warburg factor of S@Ti₃C₂Tₓ ($\sigma = 5.69$) suggests faster diffusion kinetics of Zn²⁺ ions due to facile confinement support of a 2D morphology belonging to large micro-size Ti₃C₂Tₓ ($3.40 \pm 1.2\,\mu m$). The S@C realizes a high Warburg factor ($\sigma = 6.42$), meaning a slower diffusion that may be related to the small particle size of the carbon ($0.72 \pm 0.2\,\mu m$) surrounded with inert sulfur[45].

Further, the S@Ti₃C₂Tₓ device was cycled at higher rates of 500, 700, and 1000 mA g⁻¹ and still delivered a capacity of 344, 263, and 187 mAh g⁻¹, respectively, while retaining coulombic efficiency above 90% (Fig. 3e). The polarization voltage increased significantly at the high current rate that may be related to rising in resistance

contribution. The rate capability was analyzed for 50 cycles by applying an incremental rate of 300 to 1000 mA g⁻¹ followed by a return to 300 mAh g⁻¹ (Fig. 3f). Device capacity declined to 137.2 mAh g⁻¹ at 1000 mA g⁻¹ and returned to the same performance at the initial rate, indicating facile and well-controlled energy storage. Further, the device shows stable performance for 300 cycles and retained capacity retention of 92.8% except for a few initial cycles (Fig. 3g). The fade in capacity observed here is often associated with the loss of active sulfur in aqueous media due to the formation of sulfate byproducts at the cathode surface ($2ZnS + 4H_2O + 10e^- \rightarrow 2Zn^{2+} + SO_4^{2-} + S + 8H^+$)[20,22,24]. The XPS spectra of the pristine and cycled cathode confirm the presence of sulfate and zinc in the cathode as evidenced by byproducts on the cycled cathode (Supplementary Fig. 13).

The higher active material-loaded devices were fabricated to explore the possibility of scaling of the Zn–S battery. It can also deliver a capacity of 522 mAh g⁻¹ and 400 mAh g⁻¹ for loading of 3.0 and 5.0 mg cm⁻², respectively (Supplementary Fig. 14). It was found that the capacity is linear till 1.5 mg cm⁻², but shows significant decay in capacity at loading above 2 mg cm⁻² due to possible increased internal resistance and a longer diffusion pathway[46] (Supplementary Fig. 15). It should be noted that device performance is also capacitively contributed by Ti₃C₂Tₓ, conductive carbon, and carbon cloth. For the comparison, the device with Ti₃C₂Tₓ as a cathode electrode was fabricated and tested similarly on the above devices. At a 300 mA g⁻¹ rate, the Ti₃C₂Tₓ can deliver a capacity of 65.2 mAh g⁻¹ (Supplementary Fig. 16). For the sake of comparison, the device was also prepared with a liquid electrolyte with modification in polymer content. The Zn–S battery with 5 wt% polymer content electrolyte exhibits a discharge capacity of 1016 mA g⁻¹ at 300 mA g⁻¹, with superior activation compared to
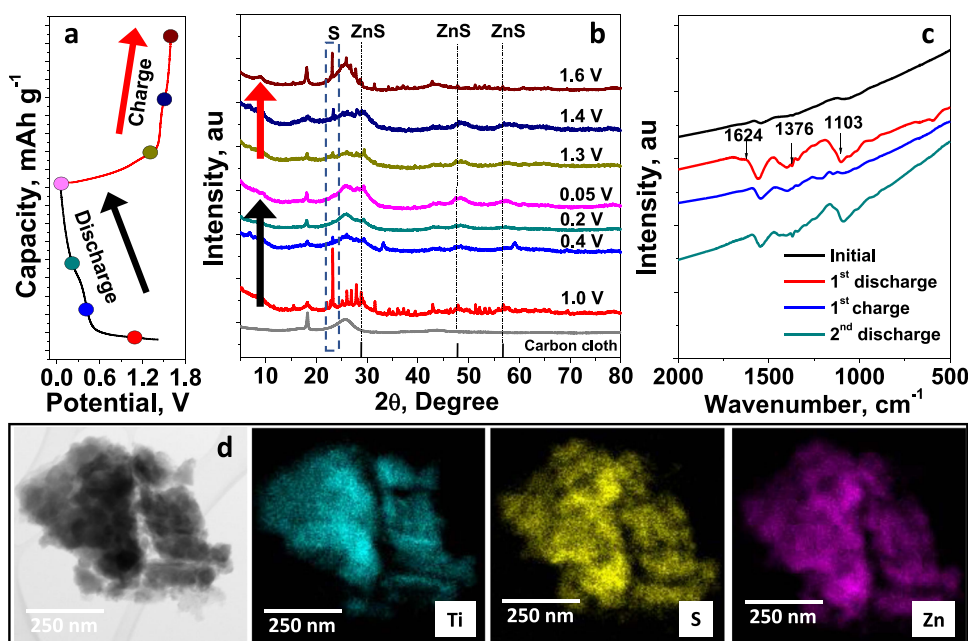
Fig. 4 Ex situ characterization of charged and discharged sulfur cathode. a, b GCD and voltage points for XRD measured during one cycle. **c** FT-IR spectroscopy for two cycles. **d** STEM and corresponding EDS elemental analysis of the discharged S@$Ti_3C_2T_x$ cathode.

AGE due to high conductivity (Supplementary Fig. 17). However, liquid electrolyte suffers from issues related to difficult sealing and leakage problems, and may not be suitable for a robust flexible device.

Investigation of zinc-ion storage in S@$Ti_3C_2T_x$

To investigate the charge–discharge mechanism of Zn storage, an ex situ spectroscopy study was adopted to identify the chemical storage conversion in the S@$Ti_3C_2T_x$ cathode by XRD, Raman, and FT-IR (Fourier-transform infrared) techniques. Figure 4a shows the typical charge–discharge voltage profile of a Zn-S battery with selected voltage points to trace the S to ZnS transformation and vice versa by XRD. The corresponding recorded X-ray diffraction patterns are provided in Fig. 4b. The representative XRD peak of S can be identified at $2\theta = 23°$ on the carbon cloth, where the broad characteristic at $2\theta = 20–30°$ arises from the carbon cloth substrate as compared in the study. First, the discharge analysis is tooled at a discharge voltage of 0.4, 0.2, and 0.05 V, where the S peak is continuously decreased while the new peaks that arise at 28°, 48°, and 56° belong to ZnS formation. This observation is in good agreement with previously reported Zn–S systems[19,23]. From 0.4 V to 0.2 V, ZnS formation starts and at 0.05 V the peaks are more intensely visible. While in charging mode from 1.3 V to 1.6 V, the ZnS peaks nearly disappear with the reformation of the sulfur peak. Here, the sulfur peak is not intense as it was in beginning, which could be related to sulfur loss during the side reaction and sulfate formation observed in the XPS study. This fact also correlates with the representative broad peak of $Ti_3C_2T_x$ nanosheet composition in the cathode, which is visible in the discharged state but is also visible in a fully charged state at 1.6 V.

These changes are also observed in Raman spectroscopy where the initial absorption characteristic of the cathode being consumed in the discharge state and reformed again in the charge state belongs to the consumption and reformation of S (Supplementary Fig. 18). The FT-IR spectra provided in Fig. 4c show the profiles of subsequent initial discharge, charge, and second discharge, which validate the reversible charge–discharge characteristics from the identified peaks of ZnS (1624, 1376, and 1103 cm^{-1})[19,47]. Those peaks are formed during the first discharge, partially disappear during charging, and then reform

again during the second charge. STEM and EDS analyses were performed for this cycled electrode to observe the distribution of discharged products and compositions. Figure 4d presents a STEM image of the discharged product of cycled cathode and corresponding EDS elemental mapping of a similar area identifies the distribution of Ti, Zn, and S elements. It can be noted that the scanning of the Zn element is identical to the S element scanning. This is evident and supports the previous observation of sulfur consumption and ZnS formation observed in spectroscopic methods.

Usually, Zn–S aqueous energy storage is benefited from sulfide shuttle-free electrochemistry compared to the Zn–MnO_2 system[23], but the use of additives like I^-/I_3^- in electrolytes may impact the battery with iodide diffusion and leads to self-discharge. However, the present Zn–S battery realizes 98.1% capacity retention after testing 27 h self-discharge rest by controlling very well the diffusion, which may be by the combined effect of AGE and $Ti_3C_2T_x$ (Supplementary Fig. 19). To understand the role of AGE and $Ti_3C_2T_x$ on the controlling self-diffusion of iodide, liquid-state Zn–S batteries of S@$Ti_3C_2T_x$ and S@C are prepared with liquid electrolyte and studied the self-diffusion in devices after the charging to 1.6 V (Supplementary Fig. 20a, b). The observed capacity retention for both cathodes is 86.01% and 90.23% for S@C and S@$Ti_3C_2T_x$, respectively, which is quite a bit lower than AGE-based devices. The lower decay observed in the S@$Ti_3C_2T_x$ suggests polar surfaces can play an important role in holding the iodides similarly observed in Zn–I_2 and Li–S batteries[34,48]. To visualize the diffusion phenomena, a liquid electrolyte-based beaker cell and an AGE-based lateral device were fabricated on a glass substrate, and biased constant at 1.6 V to monitor the iodide formation and diffusion. Supplementary Fig. 21 shows the gradual formation of iodides that later on diffused through the electrolyte and traveled to the Zn foil. In the case of AGE-based device, iodide color change was only realized at the interface of the electrode and AGE (Supplementary Fig. 22). The micro-level photograph can visualize the color formation very clearly, which is in a very short range. Further, the compatibility of Zn metal was compared with AGE and liquid-based electrolytes for the S@$Ti_3C_2T_x$ cathode to identify the role of AGE in stabilizing the Zn anode. Zn anode morphology was analyzed by SEM at the initial and then cycled in
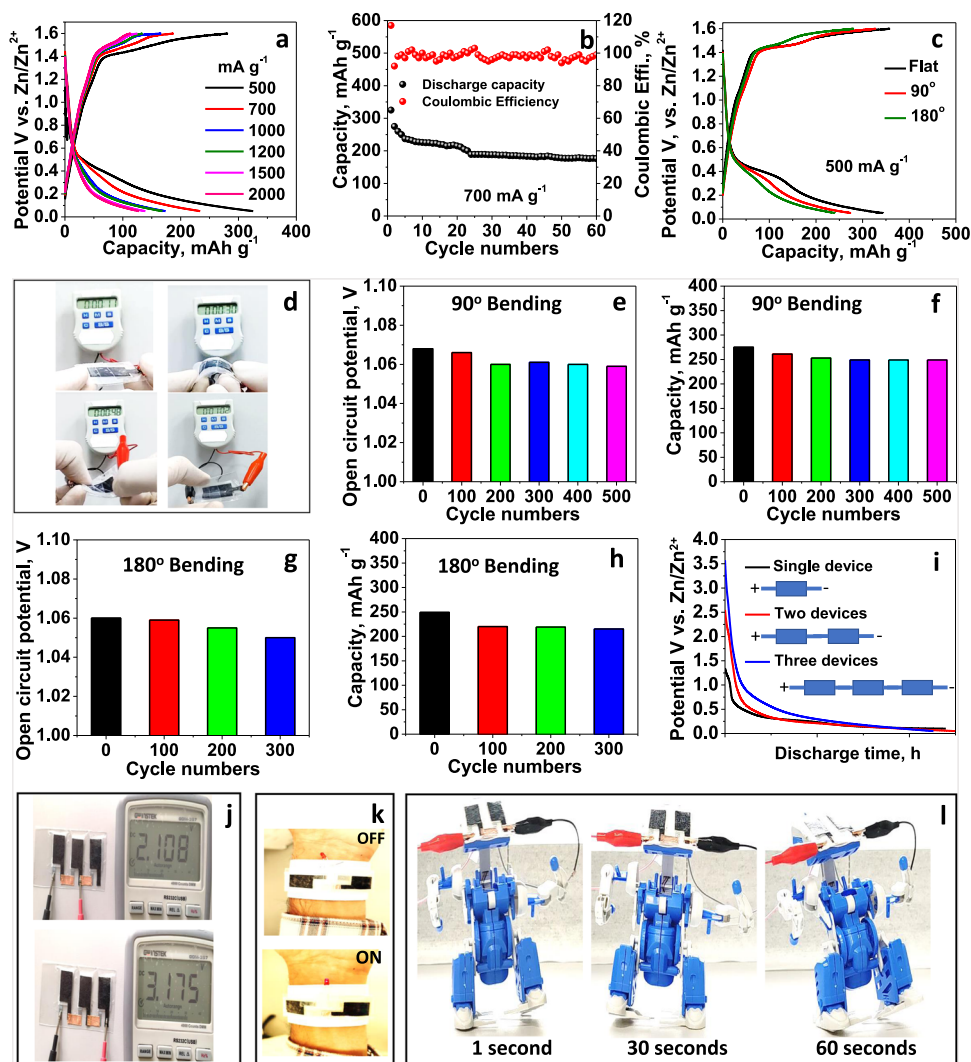
Fig. 5 Flexible Zn-S battery and real-world applications. a Charge–discharge profile of flexible Zn–S battery at different rates. **b** Stability profile of the flexible Zn–S battery. **c** Specific capacity of the flexible Zn–S battery at flat, 90°, and 180° bending. **d** Powering of a digital clock upon different bending operation of flexible Zn–S battery. **e–h** Flexibility analysis of devices at long-term bending cycles in terms of OCP and capacity retention. **i** Discharge profile of series-connected flexible Zn–S batteries. **j** Digital photographs showing the voltage of series-connected flexible Zn–S battery. Real-world applications of flexible Zn-S battery. **k** Powering of LED gadget with flexible Zn–S battery module. **l** DC motor-operated toy robot powered with Zn-S battery module.

both electrolytes (Supplementary Fig. 23). The Zn anode in AGE shows a uniform surface at the initial state that becomes layered after long-term cycling due to Zn stripping and plating events. This indicates that the electrolyte is much more suitable with a Zn anode. In the case of liquid electrolytes, the SEM image of Zn was observed with unevenly grown solid clusters on the surface. This observation suggests that the AGE and $Ti_3C_2T_x$ effectively contribute to advancing the Zn-S battery.

Flexible Zn–S battery and applications
To evaluate the flexibility of this device, the fabrication of a Zn–S flexible battery was prepared by attaching Zn foil to the flexible plastic substrate to provide a flexible backbone. Figure 5a shows the rate capability of flexible Zn–S battery at different current densities ranging from 500 mA g^{-1} to 2000 mA g^{-1}. The capacity decreases with increasing current density, reaching up to 325 mA g^{-1} at a slow rate and 137 mA g^{-1} at a faster rate. The flexible battery shows the ideal charge–discharge redox profile observed in the model coin cell device (Fig. 3e). During the long-term stability at 700 mA g^{-1}, it takes nearly 20 cycles to achieve

stable performance and then retains 82.7% capacity with average coulombic efficiency of 98.3% (Fig. 5b). The faster current rate along with scaled electrodes makes an impact on degradation in capacity belonging to possible enhanced side reactions and charge losses. The performance and stability of the flexible Zn–S battery are quite superior and comparable to that reported for flexible solid-state ZIBs with metal oxide cathodes and sulfur cathodes (Supplementary Tables 1 and 2).

Flexibility analysis was performed by cycling the battery device at 90° and 180° bending conditions with a 500 mA g^{-1} rate where capacity performance was retained at 81% and 72%, respectively, compared to the flat device (Fig. 5c). Figure 5d illustrates the demonstration of the practicality of a flexible device with flat, bent in an upward and down directions, and twisted while powering a digital clock with it (Supplementary Movie 1). The device ran undisturbed during the operation, which suggests the compactness of the electrodes/electrolyte interfaces. To validate flexibility in terms of energy storage performance, the device was evaluated by monitoring the OCP and specific capacity at 90° for 500 bending cycles (Fig. 5e, f). It retains its OCP very well with stable

capacity measured at every 100 intervals and finally reaches 91% capacity retention. Further, the device was subjected to extreme 180° bending for more than 300 cycles and still achieved 86% capacity retention (Fig. 5g, h). Overall, the device demonstrated good flexibility and electrochemical performance.

The developed flexible Zn–S battery has the potential for wearable applications and to run electronic gadgets due to its high capacity and flexibility. Owing to good energy density, the discharge voltage of this battery realizes delivering power at a very low voltage, which may limit the applicability. To enable it for practical application, we investigated a Zn–S battery module prepared by series connection of cells to achieve higher output voltage. The prepared module possesses good flexibility as demonstrated (Supplementary Fig. 24). Series-connected devices discharge curves and corresponding OCP are provided in Fig. 5i, j. In comparison to a single device with a working voltage of 1.065 V, the two and three devices connected in series exhibit 2.1 V and 3.2 V, respectively, with similar discharge times. The discharge voltage profile also showed periodic enhancement in the voltage, mainly improved initially, which could be helpful to trigger high-voltage gadgets. However, the quick voltage decay after initial gain may attribute to the increased external resistance of module devices. For the demonstration, a wearable wrist belt of two series-connected Zn–S batteries was prepared to successfully illuminate a red-colored LED indicator and power it for over 5 min (Fig. 5k). Nowadays, automotive robotics run on DC motors powered by rigid lithium-ion batteries that limit portability and present safety and cost issues. Here, for demonstration and to highlight the potential of a flexible Zn–S battery with low-cost components, we powered a toy robot equipped with a 1.5 V DC motor. The flexible Zn–S battery module designed here can power and run the toy robot for 30–60 s with two devices (Fig. 5l and Supplementary Movie 2). This demonstration application proves that systematic large-scale module design and development could efficiently solve the powering of robotics with this low-cost, flexible Zn–S battery.

In this work, $Ti_3C_2T_x$ was decorated with S to use as cathode along with AGE to improve the performance of flexible Zn-S batteries. Illustrations of two compositions of $S@Ti_3C_2T_x$ and $S@C$ elucidate the impact of $Ti_3C_2T_x$ in Zn–S redox improvement where it plays an important role to increase the redox kinetics, controlling soluble iodide shuttling by polar surface and providing a backbone for faster Zn^{2+} diffusion channels. It is concluded that the AGE coupled with $S@Ti_3C_2T_x$ cathode enables control of self-discharge and also protects the Zn anode against corrosion. The device of the $S@Ti_3C_2T_x$ cathode performs with a high energy density of 363.16 Wh kg^{-1}, which is impressive compared to metal oxide-based intercalation cathodes popular for ZIBs. The flexibility and bending study showed good performance after many deformations without significant deterioration of capacity. For the first time, strategic real-scale applications of the flexible and wearable Zn–S battery modules are demonstrated to run an LED display and power a motorized fabricated down-scale robot by connecting Zn–S batteries in series. This case study and work represent a low-cost option for future wearable devices and also a green source of energy for automotive robotics.

METHODS

Preparation of $S@Ti_3C_2T_x$ composites

$S@Ti_3C_2Tx$ composite (60 wt% S) was prepared by in situ solution-sheared method by modification in the previously reported method[49]. First, surfactant solution was prepared in mixed solvent methanol (40 v%) and chloroform (60 v%) by adding surfactant sodium cholate (2 mg/mL). According to the requirement of S and $Ti_3C_2T_x$ composition, the weight of both components in wt/wt% was added to the surfactant solution where the concentration of

$Ti_3C_2T_x$ was kept at 3 mg/mL. The resultant solution was sheared at 15,000 rpm for 45 min (15 min, 3 times at 10-min intervals) in an ice bath with a stainless steel blade stirrer from IKA. The blended solution was then taken for solvent evaporation under stirring at 50 °C. The dried mass was poured into the methanol and washed three times to remove sodium cholate from the composite followed by drying for 12 h at 60 °C. The dried mass contains the proportional composition weight added to the solution. A similar procedure was used to prepare the $S@C$ (~ 60 wt% S) sample by replacing carbon powder with $Ti_3C_2T_x$.

Preparation of amphiphilic gel electrolyte (AGE)

Amphiphilic gel electrolyte was prepared by following our previous method[33]. 1 M aqueous zinc acetate solution was prepared with 0.20 wt% iodine additive and mixed with 30 wt% (w/w) P123 pluronic block-copolymer[37,38]. Briefly, the polymer was allowed to dissolve in solution for 3 h followed by gentle mixing with a spatula. Further, the gel was subjected to three cooling–heating cycles (0 °C/25 °C) for sol-gel transitions to achieve a uniform gel phase electrolyte. For the battery application, a cellulose separator was infused in the sol state to achieve a uniformly coated separator at room temperature in the gel state.

Fabrication of electrodes and battery

The cathode was prepared on carbon cloth using a slurry coating method. At first, as-prepared active material (80 wt%) and carbon black (10 wt%) were mixed well in a mortar for 30 min, and then the slurry was prepared in NMP with PVDF (10 wt%) for a further 30 min of mixing. The homogenized slurry was doctor-bladed on the carbon cloth and dried at 70 °C for 24 h. The dried electrode was then uniformly pressed well and cut into a 1 cm^2-sized piece. The active S loading of electrodes varied from 0.8 to 1.0 mg cm^{-2} for low loading, 3.0 to 5.0 mg cm^{-2} for high loading, and 1.0 to 1.5 mg cm^{-2} for the flexible battery and modules. The Zn foil was used as an anode and polished to remove the oxide layer. The battery cell was fabricated in 2032 coin cells wherein the first-placed Zn foil was followed by a drop of sol-phase electrolyte and electrolyte-infused separator. Finally, the cathode was placed on top of the separator and the device was sealed. Further, two cooling–heating cycles (0 °C/25 °C) were applied to achieve enough penetration of electrolyte and uniform interfaces. In the flexible device fabrication electrodes were scaled to 3 cm^2. An anode was stuck on the flexible PET substrate followed by the placement of the gel-infused separators and cathode. The sandwich assembly was sealed with glue tape with three layers to make it leak-proof. The device was allowed to stabilize for 12 h before observing measurements.

DATA AVAILABILITY

The data that support the findings of this study are available from the corresponding author upon reasonable request.

REFERENCES

1. Lee, S., Hwang, J., Song, W.-J. & Park, S. Toward high energy density aqueous zinc-ion batteries: recent progress and future perspectives. *Batteries Supercaps* **5**, e202200237 (2022).
2. Zhang, T. et al. Fundamentals and perspectives in developing zinc-ion battery electrolytes: a comprehensive review. *Energy Environ. Sci.* **13**, 4625–4665 (2020).

3. Jia, X., Liu, C., Neale, Z. G., Yang, J. & Cao, G. Active materials for aqueous zinc ion batteries: synthesis, crystal, structure, morphology, and electrochemistry. *Chem. Rev.* **120**, 7795–7866 (2020).

4. Dong, H. et al. Insights on flexible zinc-ion batteries from lab research to commercialization. *Adv. Mater.* **33**, 2007548 (2021).

5. Li, N. et al. Highly flexible MnO₂@polyaniline core-shell nanowire film toward substantially expedited zinc energy storage. *Chem. Eng. J.* **452**, 139408 (2023).

6. Han, Q. et al. Durable, flexible self-standing hydrogel electrolytes enabling high-safety rechargeable solid-state zinc metal batteries. *J. Mater. Chem. A* **6**, 23046–23054 (2018).

7. Ma, Y. et al. Nanostructured polyaniline–cellulose papers for solid-state flexible aqueous Zn-ion battery. *ACS Sustain. Chem. Eng.* **6**, 8697–8703 (2018).

8. Zhao, J. et al. High-performance flexible quasi-solid-state Zinc-ion batteries with layer-expanded vanadium oxide cathode and Zinc/stainless steel mesh composite anode. *Nano Energy* **62**, 94–102 (2019).

9. Sungjemmenla, Soni, C. B., Vineeth, S. K. & Kumar, V. Exploration of the unique structural chemistry of sulfur cathode for high-energy rechargeable beyond-Li batteries. *Adv. Energy Sustain. Res.* **3**, 2100157 (2022).

10. Liu, J. et al. Sulfur-based aqueous batteries: electrochemistry and strategies. *J. Am. Chem. Soc.* **143**, 15475–15489 (2021).

11. Luo, L. W. et al. A Zn–S aqueous primary battery with high energy and flat discharge plateau. *Chem. Commun.* **57**, 9918–9921 (2021).

12. Liu, D. et al. A durable ZnS cathode for aqueous Zn-S batteries. *Nano Energy* **101**, 107474 (2022).

13. Xu, Z. et al. The key role of concentrated Zn(OTF)₂ electrolyte in the performance of aqueous Zn–S batteries. *Chem. Commun.* **58**, 8145–8148 (2022).

14. Liu, J., Ye, C., Wu, H., Jaroniec, M. & Qiao, S. Z. 2D mesoporous zincophilic sieve for high-rate sulfur-based aqueous zinc batteries. *J. Am. Chem. Soc.* **145**, 5384–5392 (2023).

15. Dai, C. et al. Maximizing energy storage of flexible aqueous batteries through decoupling charge carriers. *Adv. Energy Mater.* **11**, 2003982 (2021).

16. Dai, C. et al. A cascade battery: coupling two sequential electrochemical reactions in a single battery. *Adv. Mater.* **33**, 2105480 (2021).

17. Li, W., Wang, K. & Jiang, K. A low cost aqueous Zn-S battery realizing ultrahigh energy density. *Adv. Sci.* **7**, 2000761 (2020).

18. Amiri, A., Sellers, R., Naraghi, M. & Polycarpou, A. A. Multifunctional quasi-solid-state zinc−sulfur battery. *ACS Nano* **17**, 1217–1228 (2023).

19. Zhang, H. et al. Redox catalysis promoted activation of sulfur redox chemistry for energy-dense flexible solid-state Zn–S battery. *ACS Nano* **16**, 7344–7351 (2022).

20. Zhang, W. et al. Bidirectional atomic iron catalysis of sulfur redox conversion in high-energy flexible Zn-S battery. *Adv. Fun. Mater.* **33**, 2210899 (2023).

21. Zhao, Y. et al. Initiating a reversible aqueous Zn/sulfur battery through a "liquid film. *Adv. Mater.* **32**, 2003070 (2020).

22. Chang, G. et al. Bifunctional electrolyte additive with redox mediation and capacity contribution for sulfur cathode in aqueous Zn-S batteries. *Chem. Eng. J.* **457**, 141083 (2023).

23. Cui, M., Fei, J., Mo, F., Lei, H. & Huang, Y. Ultra-high-capacity and dendrite-free zinc−sulfur conversion batteries based on a low-cost deep eutectic solvent. *ACS Appl. Mater. Interfaces* **13**, 54981–54989 (2021).

24. Yang, M. et al. Boosting cathode activity and anode stability of Zn-S batteries in aqueous media through cosolvent-catalyst synergy. *Angew. Chem. Int. Ed.* **61**, e202212666 (2022).

25. Zhou, T. et al. Regulating uniform nucleation of ZnS enables low-polarized and high stable aqueous Zn-S batteries. *Mater. Today Energy* **27**, 101025 (2022).

26. Javed, M. S. et al. The emergence of 2D MXenes based Zn-ion batteries: recent development and prospects. *Small* **18**, 2201989 (2022).

27. Li, X. et al. Mxene chemistry, electrochemistry and energy storage applications. *Nat. Rev. Chem.* **6**, 389–404 (2022).

28. Liu, Y. et al. Sulfonic-group-grafted Ti₃C₂Tx MXene: a silver bullet to settle the instability of polyaniline toward high-performance Zn-ion batteries. *ACS Nano* **15**, 9065–9075 (2021).

29. Qi, M. et al. Three-dimensional interconnected ultrathin manganese dioxide nanosheets grown on carbon cloth combined with Ti₃C₂Tₓ MXene for high-capacity Zinc-ion batteries. *J. Colloid Interface Sci.* **615**, 151–162 (2022).

30. Venkatkarthick, R. et al. Vanadium-based oxide on two-dimensional vanadium carbide MXene (V₂Oₓ@V₂CTₓ) as cathode for rechargeable aqueous zinc-ion, batteries. *ACS Appl. Energy Mater.* **3**, 4677–4689 (2020).

31. Zhao, F. et al. In situ constructing amorphous V₂O₅@Ti₃C₂Tₓ heterostructure for high-performance aqueous zinc-ion batteries. *J. Power Sources* **544**, 231883 (2022).

32. Shi, M. et al. 3D assembly of MXene-stabilized spinel ZnMn₂O₄ for highly durable aqueous zinc-ion batteries. *Chem. Eng. J.* **399**, 125627 (2020).

33. Liang, P. et al. Heterogeneous interface-boosted zinc storage of H₂V₃O₈ nanowire/Ti₃C₂Tₓ MXene composite toward high-rate and long cycle lifespan aqueous zinc-ion batteries. *Energy Stor. Mater.* **50**, 63–74 (2022).

34. Li, X. et al. Enhanced redox kinetics and duration of aqueous I₂/I− conversion chemistry by Mxene confinement. *Adv. Mater.* **33**, 2006897 (2021).

35. Sonigara, K. K., Zhao, J., Machhi, H. K., Cui, G. & Soni, S. S. Self-assembled solid-state gel catholyte combating iodide diffusion and self-discharge for a stable flexible aqueous Zn–I₂ battery. *Adv. Energy Mater.* **10**, 2001997 (2020).

36. Machhi, H. K., Sonigara, K. K., Bariya, S. N., Soni, H. P. & Soni, S. S. Hierarchically porous metal−organic gel hosting catholyte for limiting iodine diffusion and self-discharge control in sustainable aqueous zinc−I₂ batteries. *ACS Appl. Mater. Interfaces* **13**, 21426–21435 (2021).

37. Bao, W. et al. Facile synthesis of crumpled nitrogen-doped Mxene nanosheets as a new sulfur host for lithium–sulfur batteries. *Adv. Energy Mater.* **8**, 1702485 (2018).

38. Zhao, J. et al. A smart flexible zinc battery with cooling recovery ability. *Angew. Chem. Int. Ed.* **56**, 7871–7875 (2017).

39. Sonigara, K. K. et al. A smart flexible solid state photovoltaic device with interfacial cooling recovery feature through thermoreversible polymer gel electrolyte. *Small* **14**, 1800842 (2018).

40. Li, M. et al. Halogenated Ti₃C₂ MXenes with electrochemically active terminals for high-performance zinc ion batteries. *ACS Nano* **15**, 1077–1085 (2021).

41. Li, X. et al. Vertically aligned Sn⁴⁺ preintercalated Ti₂CTₓ MXene sphere with enhanced Zn ion transportation and superior cycle lifespan. *Adv. Energy Mater.* **10**, 2001394 (2020).

42. Zhu, X. et al. Superior-performance aqueous zinc-ion batteries based on the in situ growth of MnO₂ nanosheets on V₂CTₓ MXene. *ACS Nano* **15**, 2971–2983 (2021).

43. Shi, J. et al. The high-performance MoO₃₋ₓ/MXene cathodes for zinc-ion batteries based on oxygen vacancies and electrolyte engineering. *Nano Energy* **91**, 106651 (2022).

44. Bard, A. J. & Faulkner, L. R. *Electrochemical Methods*. 2 Edn., 211 (JOHN WILEY & SONS, INC. 2001).

45. Bläubaum, L. et al. Impact of particle size distribution on performance of lithium-ion batteries. *Chem. Electro Chem.* **7**, 4755–4766 (2020).

46. Kim, Y. et al. Investigation of mass loading of cathode materials for high energy lithium-ion batteries. *Electrochem. Commun.* **147**, 107437 (2023).

47. Wang, M., Zhang, Q., Hao, W. & Sun, Z.-X. Surface stoichiometry of zinc sulfide and its effect on the adsorption behaviors of xanthate. *Chem. Cent. J.* **5**, 732011 (2011).

48. Pai, R. et al. Tuning functional two-dimensional Mxene nanosheets to enable efficient sulfur utilization in lithium-sulfur batteries. *Cell Rep. Phys. Sci.* **2**, 100480 (2021).

49. Mayorga-Martinez, C. C., Gusmão, R., Sofer, Z. & Pumera, M. Pnictogen-based enzymatic phenol biosensors: phosphorene, arsenene, antimonene, and bismuthene. *Angew. Chem. Int. Ed.* **58**, 134–138 (2019).

ACKNOWLEDGEMENTS

AUTHOR CONTRIBUTIONS

K.K.S.: material preparation, device fabrication, electrochemistry, data analysis of BET, XRD, TEM, and Raman (measured at UCT central facility), XPS measurement and analysis (CEITEC Nano), and writing the original draft; J.V.V.: SEM and EDS measurements, gadget resources, and writing original draft; C.C.M.-M.: conceptualization, supervision, and revised original draft; M.P.: financial support, methodology, supervision, initiated and oversaw the project. All authors contributed to writing the manuscript.

COMPETING INTERESTS

The authors declare no competing interests.

ADDITIONAL INFORMATION

Supplementary information The online version contains supplementary material available at https://doi.org/10.1038/s41699-023-00411-2.

Correspondence and requests for materials should be addressed to Martin Pumera.

Reprints and permission information is available at http://www.nature.com/reprints

Publisher's note Springer Nature remains neutral with regard to jurisdictional claims in published maps and institutional affiliations.